



UNIVERSITY OF LEEDS

This is a repository copy of *Micro-to nano-scale characterisation of polyamide structures of the SW30HR RO membrane using advanced electron microscopy and stain tracers*.

White Rose Research Online URL for this paper:
<http://eprints.whiterose.ac.uk/129266/>

Version: Accepted Version

Article:

Kłosowski, MM, McGilvery, CM, Li, Y et al. (5 more authors) (2016) Micro-to nano-scale characterisation of polyamide structures of the SW30HR RO membrane using advanced electron microscopy and stain tracers. *Journal of Membrane Science*, 520. pp. 465-476. ISSN 0376-7388

<https://doi.org/10.1016/j.memsci.2016.07.063>

(c) 2016, Elsevier B.V. This manuscript version is made available under the CC BY-NC-ND 4.0 license <https://creativecommons.org/licenses/by-nc-nd/4.0/>

Reuse

This article is distributed under the terms of the Creative Commons Attribution-NonCommercial-NoDerivs (CC BY-NC-ND) licence. This licence only allows you to download this work and share it with others as long as you credit the authors, but you can't change the article in any way or use it commercially. More information and the full terms of the licence here: <https://creativecommons.org/licenses/>

Takedown

If you consider content in White Rose Research Online to be in breach of UK law, please notify us by emailing eprints@whiterose.ac.uk including the URL of the record and the reason for the withdrawal request.



eprints@whiterose.ac.uk
<https://eprints.whiterose.ac.uk/>

1 Micro- to nano-scale characterisation of polyamide
2 structures of the SW30HR RO membrane using
3 advanced electron microscopy and stain tracers
4

5 Michał M. Kłosowski¹, Catriona M. McGilvery¹, Yuqiong Li²,
6 Patricia Abellan³, Quentin Ramasse³, João T. Cabral², Andrew G.
7 Livingston², and Alexandra E. Porter^{1*}

8
9 ¹ Department of Materials and Engineering, Imperial College London,
10 London

11 ² Department of Chemical Engineering, Imperial College London,
12 London

13 ³ SuperSTEM Laboratory, Daresbury
14

15 *Corresponding author: Alexandra E. Porter, Department of Materials
16 and Engineering, Imperial College London, Royal School of Mines,
17 South Kensington Campus, London, SW7 2AZ, UK; phone:
18 (+44)207594 9691; e-mail: a.porter@imperial.ac.uk
19

1 **Abstract**

2 The development of new reverse osmosis (RO) membranes with
3 enhanced performance would benefit from a detailed knowledge of
4 the membrane structures which participate in the filtration process.
5 Here, we examined the hierarchical structures of the polyamide (PA)
6 active layer of the SW30HR RO membrane. Scanning electron
7 microscopy combined with focused ion beam milling (FIB-SEM) was
8 used to obtain the 3-D reconstructions of membrane morphology with
9 5 nm cross-sectional resolution (comparable with the resolution of
10 low magnification TEM imaging in 2D) and 30 nm slice thickness.
11 The complex folding of the PA layer was examined in 3 dimensions,
12 enabling the quantification of key structural properties of the PA
13 layer, including the local thickness, volume, surface area and their
14 derivatives. The PA layer was found to exhibit a much higher and
15 convoluted surface area than that estimated via atomic force
16 microscopy (AFM). Cross-sectional scanning transmission electron
17 microscopy (STEM) was used to observe the distribution of a tracer
18 stain under various conditions. The behaviour of stain in dry and wet
19 PA indicated that the permeation pathways have a dynamic nature and
20 are activated by water. High resolution STEM imaging of the stained
21 PA nano-films revealed the presence of <1nm pore-like structures
22 with a size compatible with free volume estimations by positron
23 annihilation lifetime spectroscopy (PALS). This study presents a
24 comprehensive map of the active PA layer across different length
25 scales (from micro- to sub-nanometer) and mechanistic insight into
26 their role in the permeation process.

27 **Keywords:**

28 RO membrane, characterisation, FIB-SEM, STEM, permeation
29
30

1. Introduction

Reverse osmosis (RO) membrane filtration is frequently utilised in water purification and recycling for domestic, industrial and agricultural purposes [1,2]. Membranes designed for molecular separations in water usually comprise a “tight” separating layer of polyamide (PA) on a more open support layer of polysulfone (PSf). The PA and PSf layers are mounted on a woven fabric backing of polyethylene (PE) or polypropylene (PP) [3,4]. The topmost PA layer is thought to play the active role in the filtration process as a molecular sieve and an ion barrier [5]. Improved knowledge of the structure and chemistry of the PA layer is required to design membranes, which achieve higher performance in water desalination and purification [6]. Characterisation of the PA layer is particularly challenging due to its complex and interconnected ridge-valley structure, thinness of the active film, the sub-nanometre size of structures within the film, and beam sensitivity intrinsic to polymer materials in electron and ion beam microscopes.

The organisation of the PA layer at the meso-scale is often assessed by cross-sectional transmission electron microscopy (TEM) [7,8], isometric or top-down scanning electron microscopy (SEM) imaging [3,9–11] supported by topological information acquired via atomic force microscopy (AFM) [5,9,11,12]. The overall thickness of the PA layer ranges from 20 to 400 nm [12]. PA morphology is typically estimated by the maximum ridge-to-valley distance, average roughness and apparent surface area [5,13]. It is commonly accepted that water permeability increases with the apparent surface area of the PA layer [1].

The inner structures of the PA layer are usually characterised using electron microscopy (EM) imaging of membrane cross-sections [5]. The PA layer might be divided in two regions: a relatively flat and semi-porous base at the PA-PSf interface and a more open structure of

1 protuberances spreading from the base, giving rise to the well-known
2 ridge-valley structure [14]. Recently, it has been suggested that the
3 PA layer is formed of a continuous sub-10 nm, highly crumpled PA
4 nano-film [15]. The crumpling of the thin nano-film results in the
5 formation of multiple voids within the PA layer, especially in the
6 basal region. Some studies suggest that these voids contribute to an
7 increase in surface area (as the voids are open to the surface at one
8 end [6,16]), which might be connected with increased flux [17–19];
9 other studies suggested that the voids are discrete [19,20].

10 The molecular-scale mechanisms of particle/ion filtration are not fully
11 understood and are typically rationalised in terms of classic pore-flow
12 or solution-diffusion models [21,22]. Separation studies postulated
13 that permeation is modulated by both continuous pores and the
14 density of cross-linked polyamide [23,24]. Molecular dynamics (MD)
15 simulations suggested that the filtration occurs through a network of
16 sub-nanometre pores, which may play an active or passive role in the
17 process [25,26].

18 “Porosity” at such small length scales likely corresponds to a
19 modulation of density and free volume inherent to polymeric
20 networks, rather than to actual pores in the macroscopic sense. In
21 addition, segmental and cooperative polymer dynamics, under
22 solvation and pressure conditions, might be expected to modulate
23 solute transport [27]. Evidence of sub-nanometre pores within the PA
24 layer has been obtained by positron annihilation lifetime spectroscopy
25 (PALS) [5,22,28] and solution permeation rate calculations [29]. Until
26 now, the only spatially resolved imaging methods used to study pores
27 smaller than 10 nm were based on the tracking of nanoparticles [30].

28 Few attempts have been made to validate the permeation models
29 (pore flow vs. solution diffusion) described above. Nanoparticles have
30 been used as contrast agents in attempts to map classic pores and/or
31 permeation pathways within the PA and PSf layers. To enhance the

1 visibility of these structures in transmission electron microscopy
2 (TEM), membranes were infiltrated with nanoparticles such as Au or
3 OsO₂ [14,30]. These studies used particles of known size to visualise
4 the crumpled topography of the PA layer [14] and to measure the
5 sizes of pores in the PA layer [30]. As the nanoparticles are often
6 inhomogenously distributed within the membranes, it is difficult to
7 observe the direct transport pathways or draw conclusions about the
8 behaviour of membranes during the filtration process. Furthermore,
9 nanoparticles of set size may not accurately reflect the size of voids
10 within the membrane, due to complex transport mechanisms, the
11 variation in the sizes of the pores or the dynamic nature of these
12 pores.

13 In addition to nanoparticles, heavy metal stains such as osmium
14 tetroxide, ruthenium tetroxide, uranyl acetate or lead citrate may be
15 used to reveal the structural features of the PA layer. By contrast to
16 nanoparticles, metal stains diffuse more homogeneously through the
17 material due to their small size (initially ionic); selectively lodge in
18 charged regions; additionally fix the material and could be delivered
19 in both liquid and vapour phases. To date, staining has mainly been
20 used to enhance contrast of membranes in TEM and map the
21 distribution of functional groups in the PA layer [7,12,14]. As most of
22 the TEM studies were conducted at relatively low magnifications, it is
23 difficult to characterise any structural features smaller than 30 nm.

24 The question of how the micro- to nano-metre scale features and their
25 morphology modulate the permeation process remain unanswered [6].
26 Spatially resolved imaging techniques, such as SEM, TEM or AFM,
27 do not provide a complete picture of the 3-dimensional (3-D)
28 architecture of the PA layer and the impact of the structures within the
29 PA on the filtration process at the micro- to nano-scale. At the sub-
30 nanometre scale, little is known about the 3-D distribution of the
31 pores, their chemistry and role in solute (water/ion) transport. PALS
32 studies provide only statistical information about the bulk of the

1 membrane and computational models generally lack validation with
2 spatially resolved experiments.

3 High resolution electron microscopy (EM) studies of RO membranes
4 are so far limited. EM has mainly been used for relatively low
5 magnification, bright-field TEM imaging showing cross-sections of
6 commercial membranes [5,14] or SEM imaging of the PA surface
7 [10,11]. However, EM methods are exceptionally well-suited to
8 provide spatially resolved maps of the hierarchical structures of the
9 polyamide layer. Advanced nanoanalytical techniques, available on
10 modern scanning TEMs (STEMs), have a spatial resolution sufficient
11 to observe structural features smaller than 1 nm.

12 The combination of tomographic EM methods allows 3-D
13 visualisation of hierarchical membrane features from the micro- to
14 nano-metre length scales. Yan et al. [16] highlighted the significance
15 of large voids (10-50 nm in diameter) within the PA layer and the
16 possible pathway in the BW30 membrane. Pacheco et al. [19] have
17 recently examined void spaces (15 to 30 nm in diameter) within the
18 PA layer of ESPA3 and SWC3 in 3-D and proposed a link between an
19 increased volume of these voids with increased permeance of the
20 membrane. A 2-D study by Lin et al. [20] estimated that these voids
21 may constitute up to 30% of the PA layer volume. The focus of our
22 work is therefore to comprehensively examine and precisely quantify
23 the structures within the PA layer envelope at the micro-scale, and
24 examine structures within the PA nano-film at the nano- to sub-nano-
25 scale with unprecedented spatial resolution.

26 We combine a range of EM techniques with heavy metal staining
27 methods to visualise the hierarchical structure of the PA layer of the
28 commercially available SW30HR (Dow Filmtec) membrane, selected
29 for its common industrial use in high rejection water desalination
30 [31].

1 Focused ion beam scanning electron microscopy (FIB-SEM) was
2 used to reconstruct the features of polyamide in 3-D with high spatial
3 resolution. Staining was used not only for contrast enhancement, but
4 also for elucidation of the PA structure, specifically for mapping the
5 nano-pores within the PA nano-film using high annular dark field
6 scanning transmission electron microscopy (HAADF-STEM; atomic
7 number, Z^2 contrast imaging). Moreover, by varying the staining
8 methods, potential permeation mechanisms in the polyamide film
9 could be proposed.

10 **2. Materials and methods**

11 **2.1. Sample preparation for electron microscopy**

12 SW30HR (Dow Chemical Company, USA) flat sheet membranes
13 were stained with RuO_4 . In general, staining improves the overall
14 contrast for electron microscopy (EM) imaging, stabilises the polymer
15 under the electron beam (by crosslinking oxidised moieties, such as
16 amide and carbonyl groups) and highlights the distribution of
17 functional groups. The varying behaviour of stain tracers in different
18 staining conditions may also reveal the permeation pathways.

19

20 $1 \times 1 \text{ cm}^2$ membrane coupons cut from a larger sheet were stained
21 using standard (as received) stabilized 0.5 wt.% aqueous solutions of
22 RuO_4 (Acros Organics, Geel, Belgium). Four different staining
23 methods were used:

- 24 I. A membrane coupon was fully immersed in liquid stain for 5
25 min and immersed in 10ml of water for 30 min;
- 26 II. The top surface of membrane coupon was exposed to the stain
27 vapours for 1 min;
- 28 III. A drop of liquid stain was placed on the top surface of
29 membrane coupon for 1 min;

1 IV. A drop of pure water was placed on the top of the
2 membrane coupon for 10 min, and then the top surface of the
3 coupon was exposed to the stain vapours for 1 min.

4 Method I was used to enhance contrast for FIB-SEM imaging (SI
5 Figure 1) to ensure that the polymer was stained throughout. Methods
6 II, III and IV were used to examine permeation pathways within the
7 PA layer by STEM. To ensure the reproducibility of the results, 3
8 samples for each of the staining conditions were prepared. The
9 combination of dry (method II) and wet techniques was used to probe
10 the transport mechanisms of ions and to highlight the role of water in
11 the permeation process. Staining was performed under ambient
12 conditions. Longer staining times (5 and 10 min) were also tested for
13 methods II-IV.

14 To prepare samples for EM, the stained samples were washed 3 times
15 with water for 5 min each to remove excess stain. Next, to dehydrate
16 the samples, they were immersed in 50%, 70%, 90% and 100%
17 aqueous solutions of ethanol (30 min each). Samples were embedded
18 in LR White Hard resin (London Resin Company, Reading, UK),
19 which was found to give the best contrast from the PA polymer.
20 Samples were immersed successively in 1:1 and 3:1 resin:ethanol
21 solutions for 12h. For the next 4 days, samples were immersed in pure
22 resin to ensure full infiltration. The resin was changed every 24h. On
23 the last day samples in resin were degassed under vacuum to ensure
24 sample-resin binding and resin hardening. The final resin batch was
25 mixed with a dedicated LR White accelerator (benzoyl peroxide) to
26 enhance the crosslinking of the resin at room temperature. Pristine
27 (non-stained) samples were embedded using the same protocol.

28 **2.2. Focused ion beam SEM (FIB-SEM)**

29 For FIB-SEM milling, a flat surface of the resin embedded sample
30 stained, using method I, was exposed using a PowerTome
31 ultramicrotome (Boeckeler Instruments, Tucson, USA) with a

1 diamond knife (DiATOME, Hatfield, USA). Next, a 1 mm thick slice
2 was cut and mounted on an aluminium stub using silver paint. Prior to
3 SEM imaging, the sample was coated with a 20 nm layer of
4 chromium to reduce charging.

5 FIB-SEM series were taken on an Auriga microscope (Carl Zeiss
6 Microscopy, Jena, Germany) fitted with a gallium ion source. The
7 FIB milling conditions were set to 30 kV and with a beam current of 1
8 nA, which results in a probe size of ~10nm.

9 Samples were milled from the side (SI Figure 2). To minimise FIB
10 damage (e.g., ion implantation and curtaining) during alignments, the
11 top, 1 μ m-thick part of sample was used as a sacrificial layer. Only the
12 region below the sacrificial layer was imaged by SEM (SI Figure 2).

13 SEM imaging was performed at 1.49 kV with an energy selective
14 backscattered electron detector. In these conditions, the size of SEM
15 probe is ~2nm. Pixel averaging collection was used to reduce noise.
16 In total, 357 images of membrane cross-sections were acquired, with
17 a step size of 30 nm between successive images. As SEM images
18 were taken at an angle (SI Figure 2), the images had to be adjusted to
19 account for this resulting in non-uniform pixels (the pixel size in y
20 direction was multiplied by 1.24).

21 Avizo software (FEI, Hillsboro, USA) was used for pre-processing of
22 FIB-SEM data and reconstruction of virtual volumes. FIB-SEM
23 slices were denoised using a Gaussian filter and realigned using an
24 automatic least-squares function. Further information on thresholding
25 and reconstruction can be found in SI (SI Figure 3). The reconstructed
26 voxel size was 3.7x4.6x30 nm³.

27 **2.3. Estimation of structural properties**

28 To minimise errors in the calculation of membrane parameters arising
29 from non-uniform voxels [32], volumes reconstructed from FIB-SEM
30 data were resliced in ImageJ [33] to obtain uniform voxels of 5x5x5

1 nm³. To accurately assess the outer volume of the PA layer envelope
2 and the impact of the discrete objects within the envelope on the
3 structural parameters, the volume was purified (discrete voids and
4 particles were removed from the volume – SI Figure 4) in BoneJ [34].
5 The PA layer is very heterogeneous; to address the natural variability
6 of the membrane, 2.5x2.5 μm² regions were examined.

7 BoneJ was used to determine the total surface area (SA), volume (V)
8 and local thickness [35] distribution of the PA layer envelope. The
9 local thickness at any given point (voxel) of a 3-D structure is defined
10 as the diameter of the largest sphere that fits inside the 3-D object and
11 contains the point [35]. In other words, the individual local thickness
12 measurement represents the local diameter of the structure. A graphic
13 explanation of the local thickness measurement is given in SI Figure
14 5. The rudimentary reactivity was estimated as surface-to-volume
15 (SA/V) ratio. Front and rear surface areas were calculated from the
16 total surface area of front and rear volumes by subtracting the side
17 and division areas (SI Figure 4). Relative area ratios were calculated
18 by dividing the actual surface area by the area of the underlying
19 rectangle.

20 **2.4. Atomic force microscopy (AFM)**

21 For comparison with the surface structure generated from FIB-SEM,
22 AFM imaging was used. The front surface of the PA layer was
23 imaged on the original SW30HR membrane taped to an AFM sample
24 holder with the PA facing upwards. To image the rear surface of the
25 PA layer, free-standing PA layers were prepared and placed on a glass
26 cover slip. The freestanding membranes were obtained as follows.

27 The polyethylene (PE) backing was carefully peeled off of the
28 SW30HR membrane with a scalpel blade. The remaining two-layered
29 membrane was pressed onto a clean glass cover slip such that the PA
30 side sticks to the glass substrate. A drop of deionized water was added
31 to hydrate and soften the membrane. A few drops of

1 dimethylformamide (DMF) were carefully placed onto the PSf facing
2 upwards. As the PSf dissolved in the solvent, the glass slide was tilted
3 to allow the solvent with the dissolved PSf to be drained. The process
4 was repeated several times until the PSf was completely removed.
5 The isolated PA thin layer appeared optically transparent.

6 Samples were imaged in an Innova AFM (Bruker, USA) in tapping
7 mode fitted with a phosphorus (n) doped silicon cantilever ($k = 20\text{-}80$
8 N/m, tip nominal diameter <10 nm). AFM images were acquired at
9 512 samples/line and a scanning rate of 0.2 Hz, under ambient
10 conditions.

11 **2.5. Scanning transmission electron microscopy (STEM)**

12 For TEM imaging, thin (~ 70 nm) sections of samples were cut with
13 the ultramicrotome (Boeckeler Instruments, Tucson, USA) and
14 transferred onto 300-mesh copper grids with a lacey carbon film
15 support (TAAB Laboratories Equipment, Aldermaston, UK).

16 STEM imaging was performed on a C_s (image-)corrected, FEI Titan
17 80-300 microscope operated at 80 and 300kV. A 60 mm camera
18 length was used giving an annular dark field (ADF)-STEM collection
19 semi-angle of 26-145 mrad and high angle (HA)ADF-STEM
20 collection semi-angle of 129-575 mrad. Before imaging, samples
21 were beam showered (exposed to an uncondensed broad electron
22 beam) in the TEM mode to stabilise the sections by equalizing the
23 charge distribution across the section and reduce hydrocarbon
24 contamination [36]. The experimental dose was closely monitored and
25 did not exceed 1250 e/nm².

26 High resolution STEM imaging was performed on SuperSTEM2 -
27 Nion UltraSTEM 100 microscope at 100kV. The HAADF collection
28 semi-angle range is 85-190 mrad and the probe size is 0.1 nm. Prior to
29 imaging, samples were baked for 12h in a vacuum oven (10^{-6} Torr)
30 with a rising temperature gradient (from room temperature to 130°C)
31 to reduce hydrocarbon contamination.

2.6. Quantification of the <1 nm structures

High resolution images were denoised using a Gaussian filter, contrast-enhanced and thresholded using magic wand selection. We aimed to highlight only structures that showed local maxima. In some instances we used a water-shedding algorithm to separate larger clusters of stain precipitates. The surface areas of the reconstructed precipitates were calculated using ImageJ (SI Figure 6). The diameters of the pores were estimated as the diameter of circles of the same area. All spots of diameter smaller than 0.2 nm were filtered out (the approximate size of Ru atoms \approx 0.15 nm).

3. Results

3.1. 3-D structure of the polyamide layer

To reconstruct and quantify features of the PA layer morphology, cross-beam FIB-SEM tomography was used. We are able to visualise features larger than 15 nm in the PA layer in 3-D. The 3-D reconstruction in Figure 1 and SI Movie 1 shows the front (Figure 1A) and rear (Figure 1B) surface, and cross-sections (Figure 1 C, D) of the PA envelope. The envelope represents a volume containing the entire PA layer with the discrete, inner voids excluded. Orthoslices taken through the 3-D reconstructions show that protuberances, which are often referred to as ridges [5], are in fact leaf-like (bridge-like) sheets overhanging large regions of the PA layer (Figure 1 C, D - arrowheads). These regions are not fully enclosed and large empty spaces directly underneath the ridges are open to the front surface. There were also smaller, discrete voids observed within the PA envelope (Figure 2 and SI Movie 2). These discrete voids have an average local thickness of 21 ± 7 nm (367 voids for the minimal threshold) and 17 ± 5 nm (61 voids for the maximal threshold).

Local thickness mapping [34] was also performed on the bulk features of the PA layer (Figure 3A, B and C). The local thickness describes dimensions of all PA layer features: from a single sheet (\sim 10 nm) to

1 multiple convoluted and compacted sheets of PA nano-film (~260
 2 nm). The latter structures appear as non-porous (Figure 3 B, E – white
 3 arrowheads), but may possess void spaces, which are below the
 4 resolution of the FIB-SEM technique or remain unresolved due to
 5 poor contrast.

6 The ridge-like features (Figure 1A and C) on the front side of the
 7 membrane were found to be <70 nm thick, whereas the features on the
 8 rear side of the PA layer were much thicker (up to 260 nm), as AFM
 9 cannot measure overhangs, steep walls and other convoluted
 10 structures of the PA topography. For comparison, AFM maps were
 11 converted into 3-D models and local thickness maps were calculated
 12 (Figure 3D, E and F). The measured root-mean square roughness was
 13 75 nm and the peak-to-peak height was 496 nm for the front surface,
 14 and 15nm and 110nm, respectively, for the back surface. In the AFM
 15 reconstruction, almost all of the membrane volume appeared thick
 16 (bright), because this method only maps the apparent topography. In
 17 Table 1, the structural properties of the PA layer in the SW30HR
 18 membrane are given.

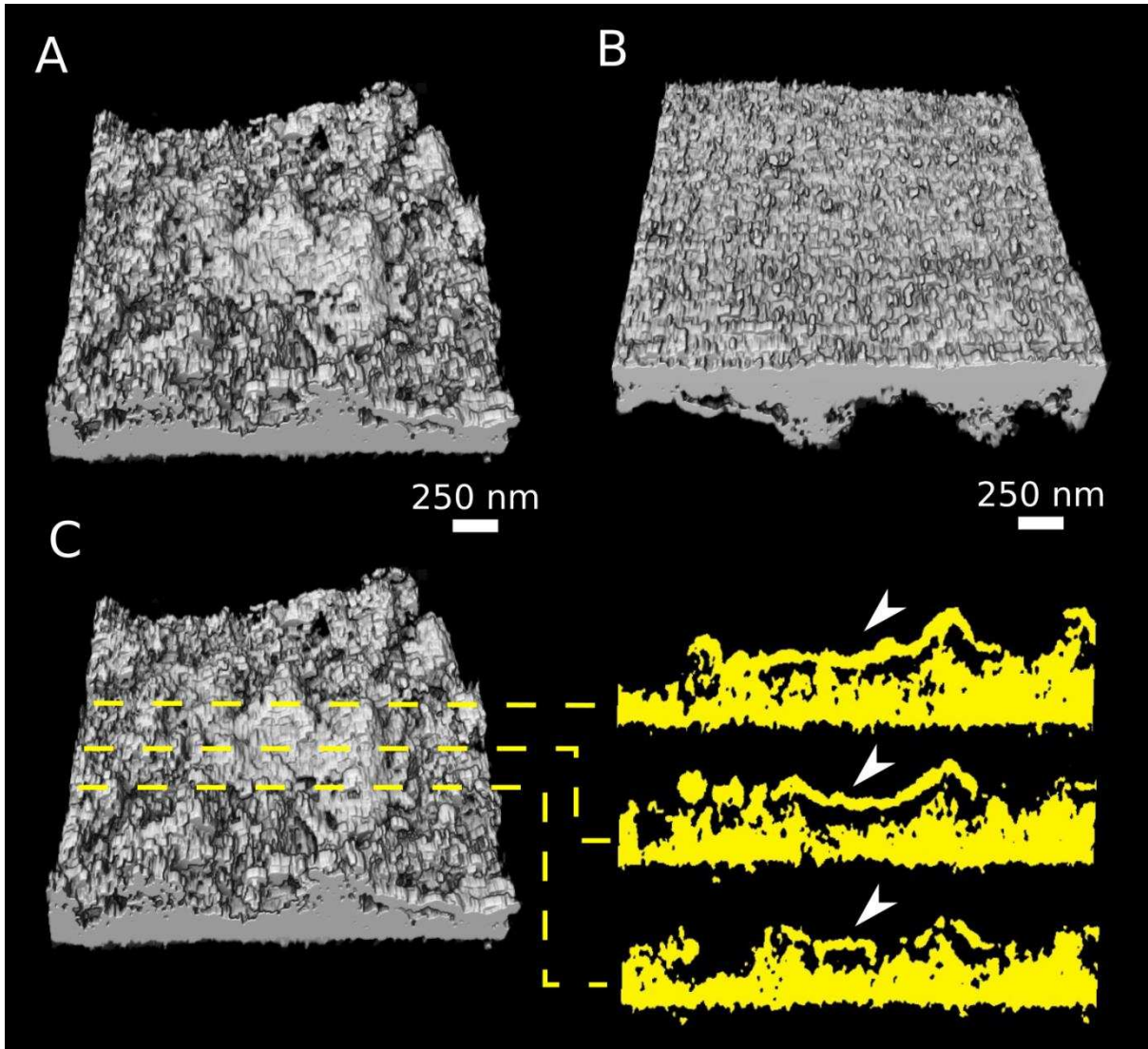
19 **Table 1 Structural properties of the PA layer of a SW30HR**
 20 **membrane (for 2.5x2.5 μm^2 regions).**

	Mean local thickness (nm)	Maximal local thickness (nm)	Reactivity SA/V (nm^{-1})	Relative area ratio - front	Relative area ratio - rear
PA envelope (MIN*)	96±42	206	0.037	6.71	1.87
PA envelope (MIN Purified)	125±61	260	0.033	5.98	1.67
PA envelope	179±92	344	0.028	4.9	3.55

(MAX)					
PA envelope (MAX Purified)	183±90	344	0.025	4.66	2.64
AFM	284±71	443	0.012	1.71	1.3**
AFM Purified	285±70	443	0.012	1.64	1.3**

1 * MIN – minimal threshold, MAX – maximal threshold, Purified –
2 discrete voids removed

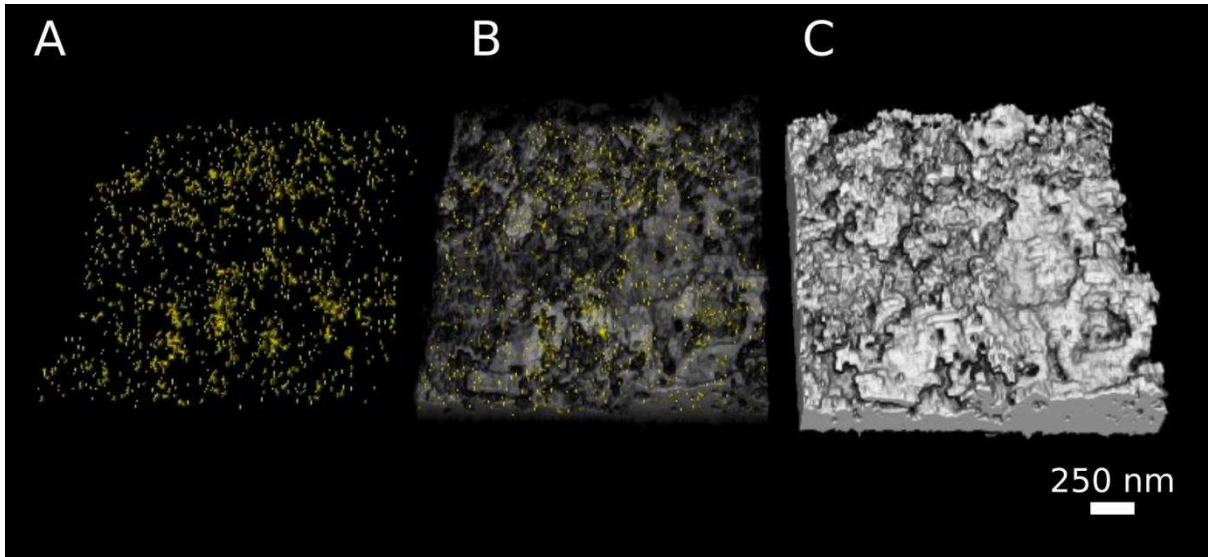
3 ** AFM front and rear surface images were collected from different
4 regions.



1

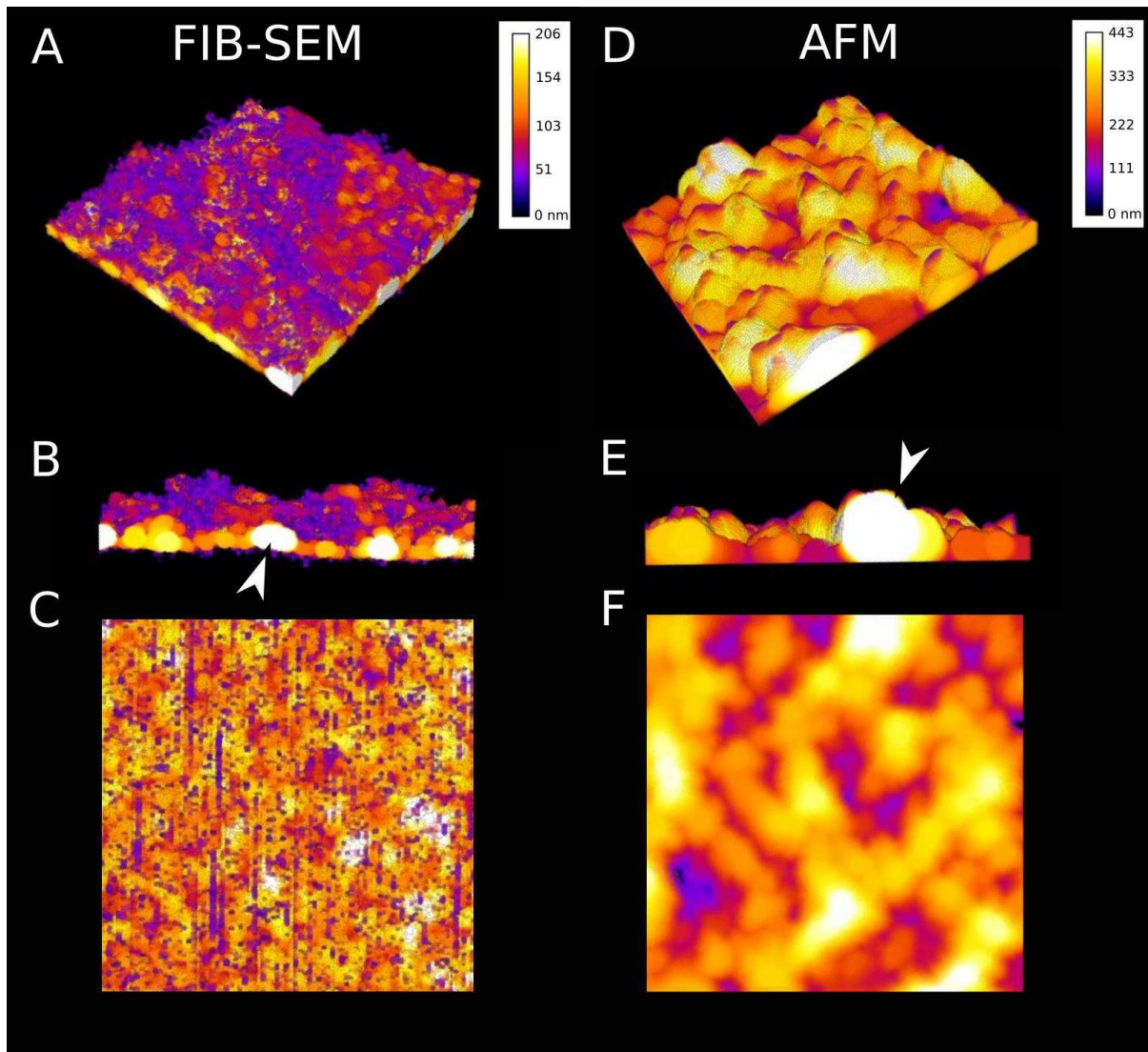
2 **Figure 1 A FIB-SEM 3-D reconstruction of the PA layer envelope**
3 **showing: (A) the front and (B) rear surfaces of the PA and (C)**
4 **cross-sections through the ridges showing that they are hollow**
5 **(white arrowheads). All voids seen in (C) are open to the surface.**

6



1

2 **Figure 2 A FIB-SEM 3-D reconstructions of discrete voids**
3 **(yellow) and the PA envelope (grey). (A) Discrete voids extracted**
4 **from the PA reconstruction through a purification routine. (B)**
5 **The same voids (A) overlaid with a semi-transparent PA**
6 **envelope. (C) A fully opaque reconstruction of the PA envelope in**
7 **the given region.**



1

2 **Figure 3 A local thickness map of the PA envelope: (A) an**
 3 **isometric, (B) side and (C) a rear view from a FIB-SEM**
 4 **reconstruction and (D) an isometric, (E) side and (F) a rear view**
 5 **from an AFM reconstruction. Thin regions are dark (red to**
 6 **violet), while thick regions are bright (white to yellow; the**
 7 **thickest structures for each reconstruction are indicated by white**
 8 **arrows). Each view shows a $2.5 \times 2.5 \mu\text{m}^2$ region.**

9 **3.2. Inner structure of PA layer**

10 Staining experiments were used to reveal the inner structures of the
 11 PA layer, seeking to resolve possible permeation pathways, and thus,
 12 transport mechanisms through the PA nano-film.

1 In Figure 4, the effects of vapour staining on a dry membrane (method
2 II) are shown. As the vapour stain reached the top surface of the
3 membrane, stain propagation was evidently hindered at the PA-air
4 boundary. The stain did not penetrate readily into the PA nano-film
5 and instead precipitated forming a bright crust along the top interface
6 (Figure 4 A, B). Bright spots within the PA nano-film were also
7 observed (Figure 4C), suggesting that some stain precipitated within
8 the pores of the PA. Many of the voids observed at the rear side of the
9 PA layer (i.e., inside the basal region next to the polysulfone support)
10 were not accessed by the stain. Stain precipitates were observed in
11 only a few of these voids (Figure 4A, arrowheads), which are most
12 likely open to the top surface. Occasionally, stain precipitates
13 aggregated at the entrance to a seemingly open void (Figure 4D and
14 SI Movie 3). In general, the propagation of stain through a dry PA
15 layer was significantly impeded.

16 The liquid staining technique (method III) sought to visualise the
17 transport of water in the PA layer. As the stain is in an aqueous
18 solution, the distribution of tracer should, in principle, reflect the
19 fraction accessible to water molecules within the PA layer. In Figure
20 5, the effects of liquid staining on the front side of the membrane are
21 shown, in clear contrast to the dry images above. When the liquid
22 stain was applied on the top surface, the stain propagated through the
23 PA layer and into the PSf support. Voids on the rear side of the PA
24 layer (towards the PA/PSf interface) and very complex structures
25 within the PA were penetrated by the stain (Figure 5 A, C). Staining
26 highlighted the presence of effective “channels” within the PA layer
27 (Figure 5 B, D), which were either filled with a dense precipitate
28 (black arrowheads) or were empty (white arrowheads). Such
29 ”channels” were also observed in non-stained samples (Figure 6), but
30 staining significantly enhanced their visibility. These structures have
31 significantly weaker contrast in the pristine (non-stained) PA, which

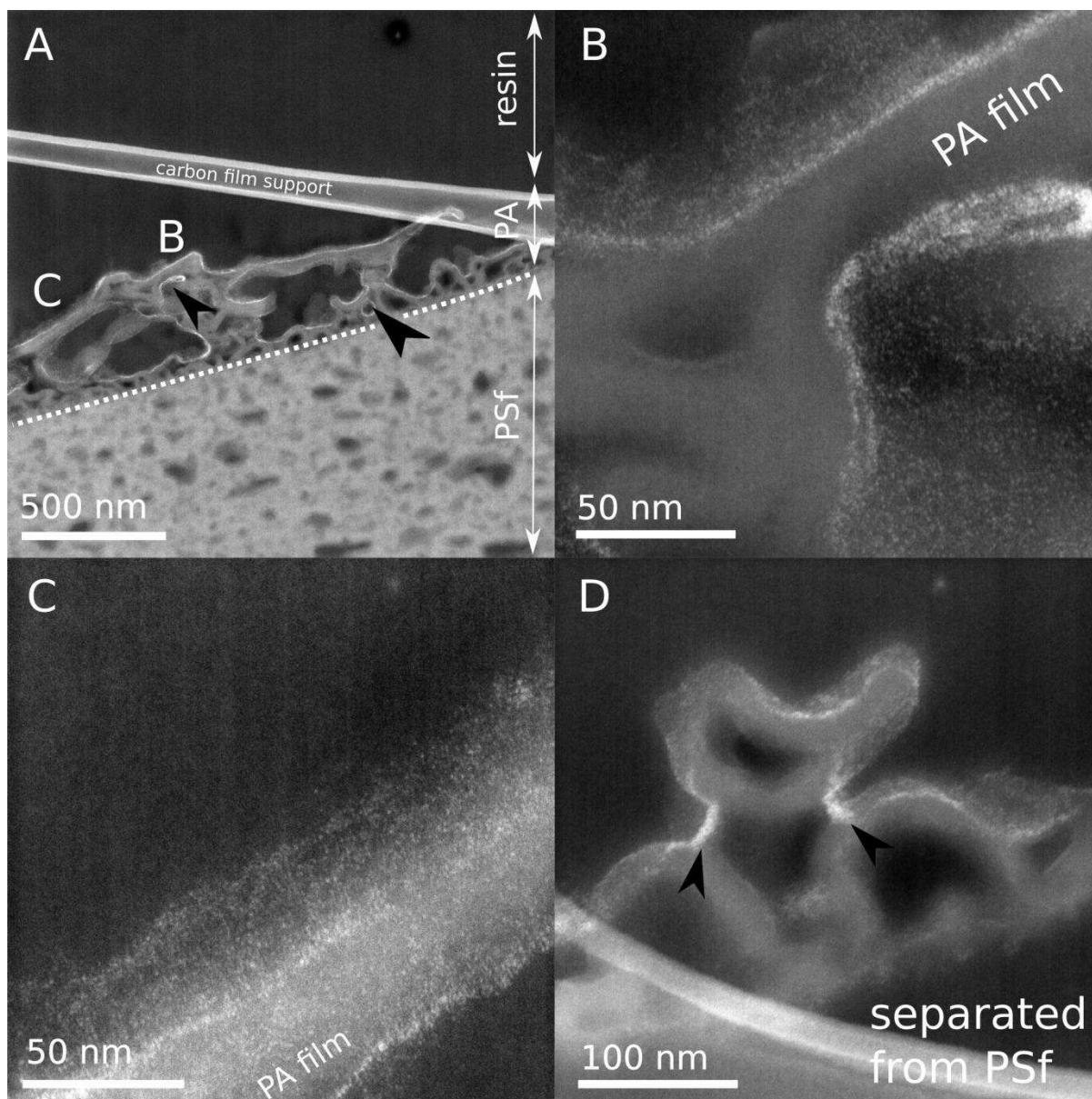
1 suggests that these are hollow regions formed by tight folding of the
2 PA film.

3 The staining patterns clearly differed between the dry and wet
4 experiments presented above. Therefore, membrane solvation and
5 swelling in water and must play a significant role in activating the
6 permeation pathways within the PA. To test this hypothesis, the
7 vapour staining technique on a wet membrane (method IV) was used
8 to further investigate the role of water and access of transport
9 pathways in the membrane. In Figure 7, the effects of vapour staining
10 on a wetted membrane were shown. In comparison to the dry
11 membrane (Figure 4) the stain started to reach enclosed regions of the
12 PA layer (Figure 7A), but did not penetrate the PA as thoroughly as
13 under wet conditions (Figure 5). Smaller precipitates within the PA
14 nano-film were often observed and occasionally, a stain propagation
15 front could be seen (Figure 7B).

16 For longer staining times (5 and 10 min), precipitates outside the PA
17 layer dominated the contrast (SI Figure 7).

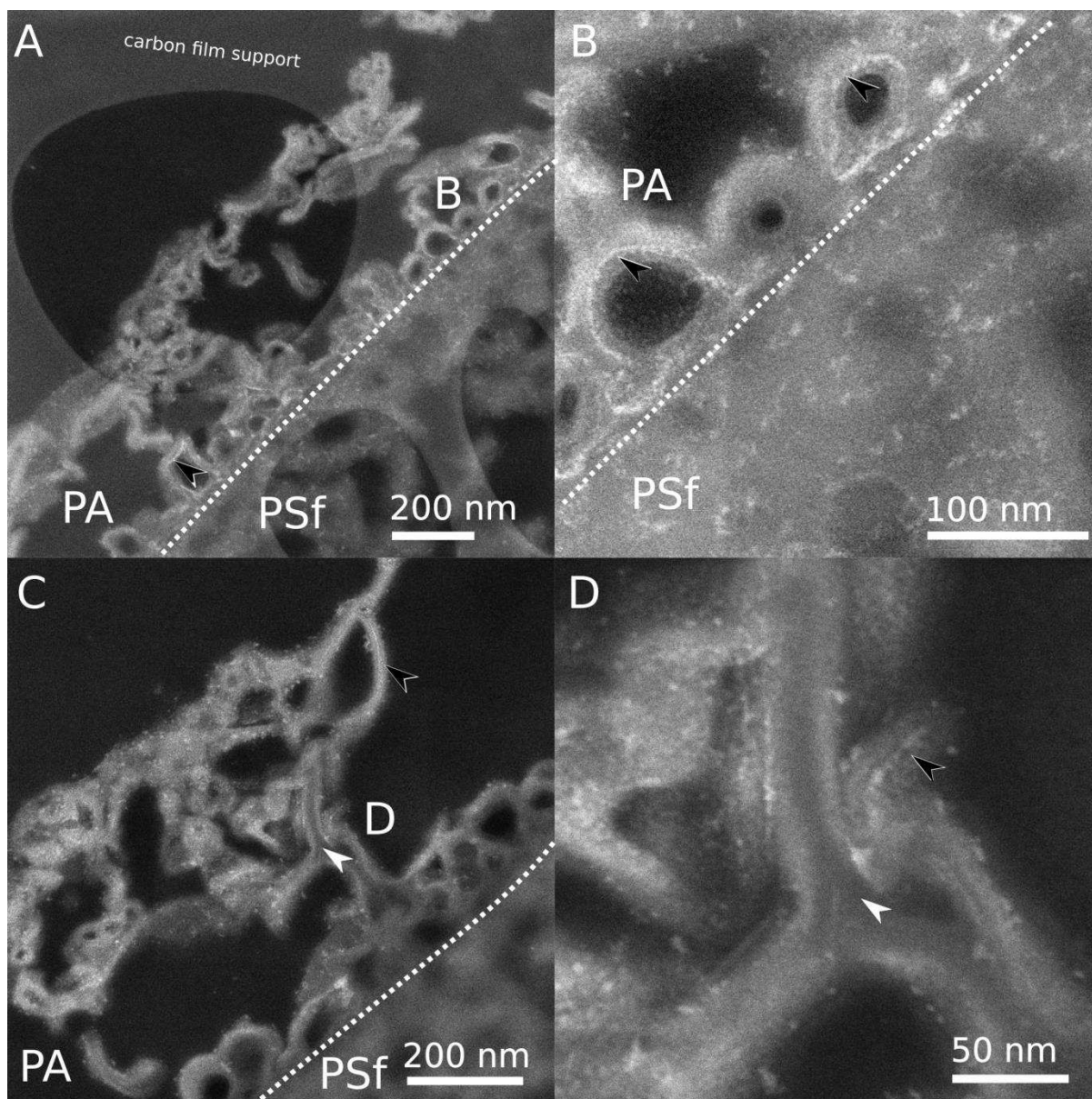
18

19



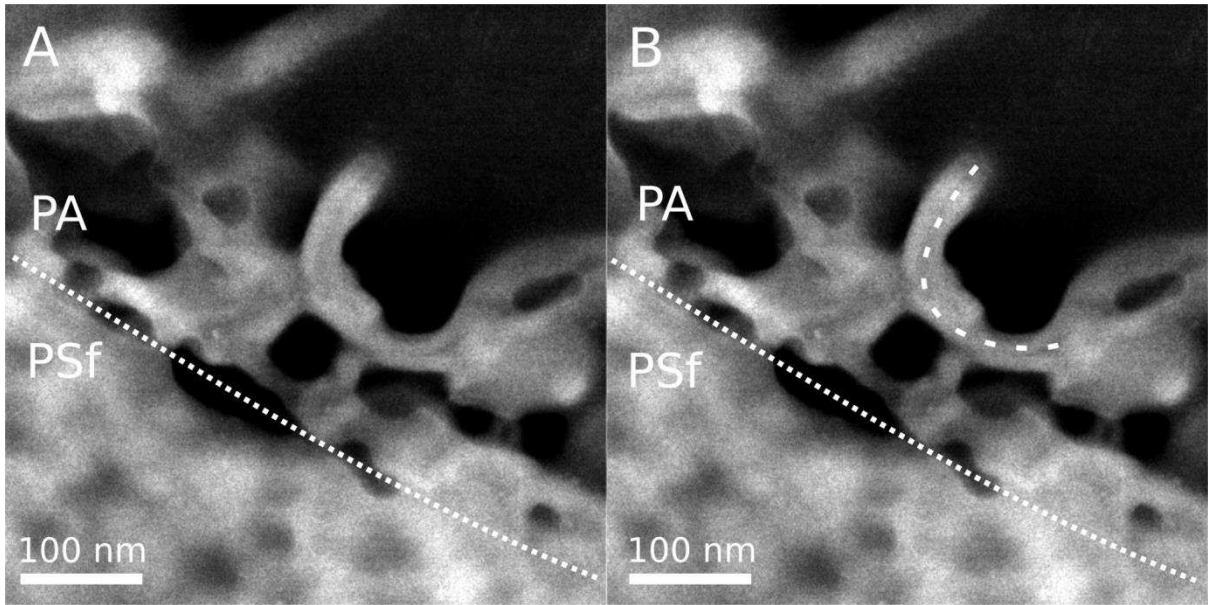
1

2 **Figure 4 HAADF-STEM images of a dry SW30HR membrane,**
 3 **which was vapour stained on the front side with RuO₄ for 1 min.**
 4 **(A) Stain precipitates formed on the surface of the PA layer and**
 5 **within few voids (black arrowheads) within the layer. The dotted**
 6 **line represents the PA/PSf interface. (B) Higher magnification**
 7 **image of the region seen in (A) showing stain on the outside of the**
 8 **nano-film. (C) Higher magnification image of the region seen in**
 9 **(A) showing stain precipitates within the PA nano-film. (D) Stain**
 10 **precipitates aggregating (black arrowheads) in the entrance to a**
 11 **seemingly open void.**



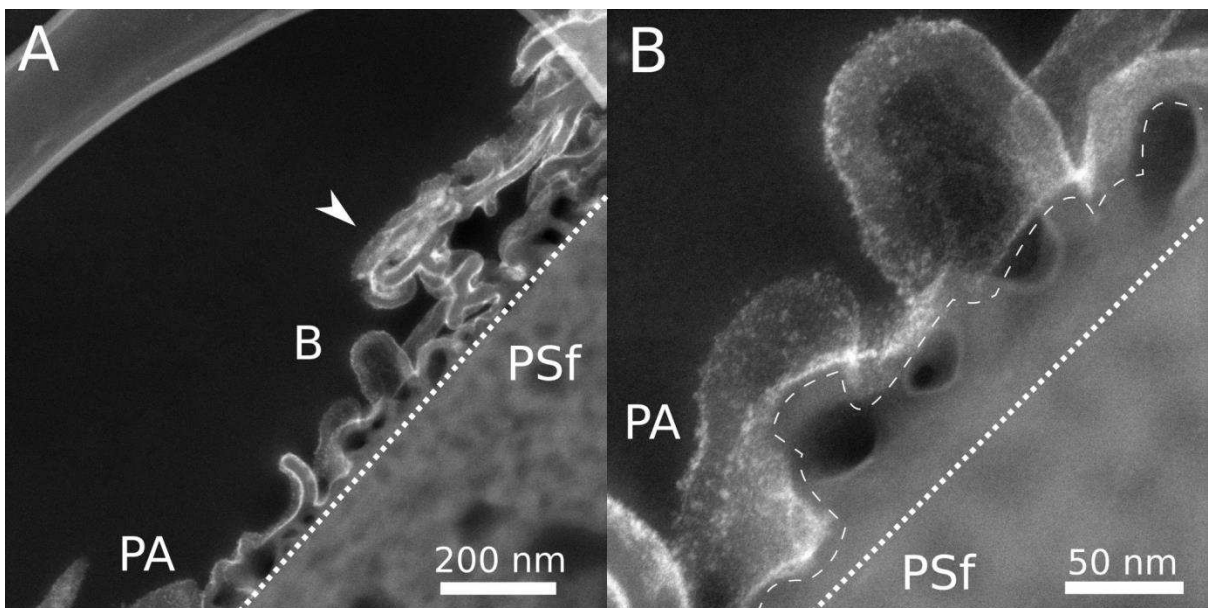
1

2 **Figure 5 HAADF-STEM images of a SW30HR membrane stained**
 3 **from the front side with RuO₄ in aqueous solution for 1 min. (A)**
 4 **Stain precipitates were present in the whole volume of the PA**
 5 **layer. (B) Higher magnification image of the region seen in (A)**
 6 **showing dense precipitates (black arrowheads) formed within**
 7 **“channels” of the basal PA layer. (C) Selective staining showing**
 8 **empty (white arrowheads) and occupied (black arrowheads)**
 9 **“channels” within the PA. (D) Higher magnification image of**
 10 **empty (white arrowheads) and filled (black arrowheads)**
 11 **channels seen in (C). The dotted lines in (A), (B) and (C)**
 12 **represent the PA/PSf interface.**



1

2 **Figure 6 HAADF-STEM images of a non-stained SW30HR**
 3 **membrane. (A) An acquisition showing empty channels within the**
 4 **PA layer. (B) A respective image with highlighted “channels” - ,**
 5 **possibly representing collapsed voids. The dotted lines in (A) and**
 6 **(B) represent the PA/PSf interface.**



7

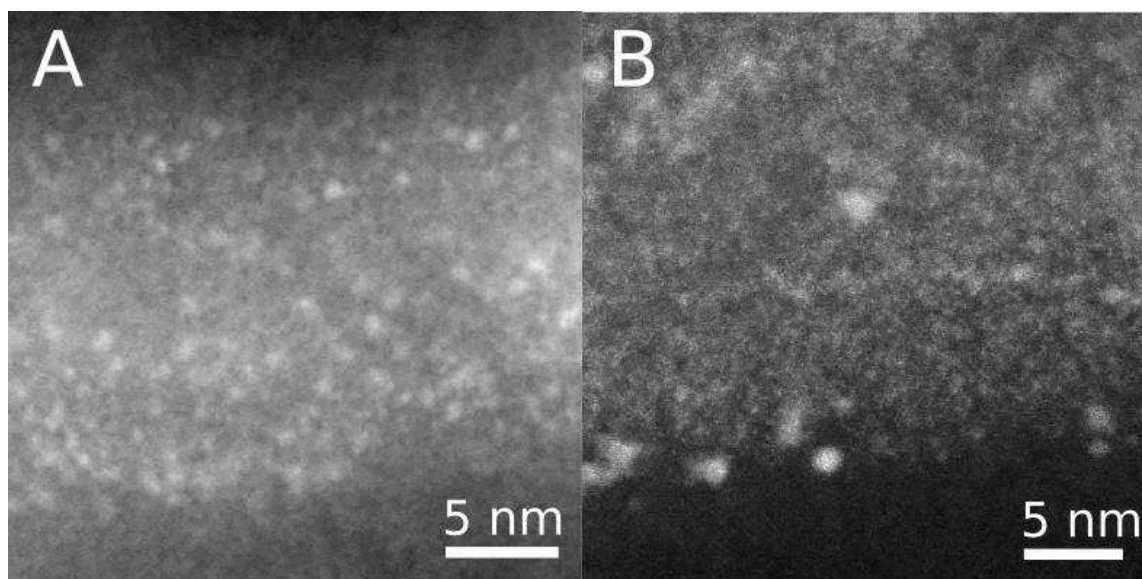
8 **Figure 7 HAADF-STEM images of a wetted SW30HR membrane,**
 9 **which was vapour stained on the front side with RuO₄ for 1 min.**
 10 **(A) Stain precipitates formed on the surface and within**
 11 **convoluted regions (white arrowhead) of the PA layer. (B) Higher**
 12 **magnification image of the region seen in (A) showing stain within**

1 **the nano-film and a stain propagation front (dashed line). The**
2 **dotted lines in (A) and (B) represent the PA/PSf interface.**

3 4 **3.3. Porosity of the polyamide nano-film**

5 Until now the presence and dimensions of sub-nanometre pores
6 within the PA nano-film have been estimated via indirect techniques,
7 such as PALS [5]. The observation of <1 nm pores has been
8 significantly hindered by intrinsic low contrast of polymer material
9 and shortcomings of imaging techniques. With the combination of
10 high spatially resolved EM imaging and staining methods described
11 above, <1 nm pores can be visualised. The stain highlights circular
12 regions within the PA nano-film (Figure 8). This contrast arises from
13 stain precipitates lodged within the nano-film.

14 For high resolution STEM imaging, regions where precipitates had
15 formed within the PA nano-film (stained with method II and III) were
16 selected. Only sections with the stain evenly distributed across the
17 cross-section were examined to ensure that the observed precipitates
18 were inside the PA nano-film and not on its surface. The micrographs
19 show the presence of precipitates within the PA nano-film (Figure 8).
20 Both images show a fragment of a PA nodule at high magnification
21 (SI Figure 8). The average diameter of precipitates formed within the
22 nano-film is <1 nm (0.7 ± 0.4 nm for vapour stained; 0.6 ± 0.4 nm for
23 liquid stained; $n=250$).



1

2 **Figure 8 HAADF-STEM images of stain precipitates in the PA**
3 **nano-films of the SW30HR membrane exposed to (A) the vapour**
4 **and (B) liquid stain for 1 min (method II and III). Both images**
5 **show cross-sections through the protuberances at high**
6 **magnification (SI Figure 8).**

7 **4. Discussion**

8 Staining combined with high resolution EM has provided several
9 important advances in our understanding of the structure-related
10 mechanisms by which the filtration occurs. Since direct, nano-scale
11 observations of RO membranes in operating conditions are so far
12 virtually impossible, we attempted to capture the changes in
13 membrane behaviour using a tracer stain. The permeation through the
14 PA layer depends on many factors, such as the accessible surface area
15 of the PA layer and the nature of transport pathways within the PA
16 layer and the 10 nm PA nano-film.

17 Using high resolution FIB-SEM 3-D reconstructions, we showed that
18 the highly complex structures of the PA layer have a much larger
19 active surface area than when examined via AFM. The behaviour of
20 tracers within the dry and wet PA highlights the role of water
21 solvation and swelling in activating the transport pathways. Finally, at
22 the sub-nano-scale, we visualised <1 nm pore-like structures within

1 the PA nano-film using heavy metal staining. These observations lead
2 to important conclusions about the membrane behaviour during the
3 permeation and the role of water during this process.

4 **4.1. 3-D reconstructions of the polyamide layer**

5 FIB-SEM was used to obtain 3-D reconstructions of membrane
6 morphology with resolution comparable with the resolution of low
7 magnification TEM imaging [14]. Discrete voids within the PA layer
8 observed with FIB-SEM correspond in size (average 20 nm) to those
9 observed in a previous electron microscopy studies [19,20]. We build
10 on the aforementioned studies by focusing on reconstruction of the
11 surrounding PA envelope and studying the distribution and
12 interconnectivity of voids within the PA envelope. Additionally, the
13 heavy metal staining methods used allowed for more robust and
14 automated thresholding, which enabled a straightforward
15 quantification of the structural parameters of the PA layer and void
16 spaces.

17
18 Large empty spaces under the ridges of the PA layer, which might be
19 easily accessible to fluids (Figure 1D), as well as smaller, discrete
20 voids within the PA envelope (Figure 2) were observed. While cross-
21 sectional studies tend to assume all voids observed in the image are
22 discrete [20], it is important to highlight that some of the voids within
23 the PA layer, which appear discrete in the 2-D cross-sectional images,
24 are open to either of the surfaces (but not both – Figure 1D, SI Movie
25 1, Figure SI 4). The presence of large empty spaces under the ridges
26 increases the active surface of the membrane, which in turn may
27 affect the water flux. The range of morphologies of the protuberances
28 and their impact on separation performance have been reported on in
29 previous studies [9,37–40], but until now have not been accurately
30 quantified. We calculated structural parameters of the PA layer such

1 as local thickness or relative area ratio and compared the results with
2 AFM data.

3 It has been shown that while AFM is commonly used in the
4 characterisation of RO membranes [37,41], it significantly
5 underappreciates the complexity of the PA layer. Using a SW30HR
6 membrane, we showed that the actual front surface area might be 2.5-
7 4 times larger than when estimated with dry AFM. Similarly, the
8 SA/V ratio might be 2-3 times greater. On the other hand, the
9 morphology of the rear side agreed with previous studies [42] and the
10 surface area of the rear sides of the PA layer was comparable between
11 FIB-SEM and AFM measurements.

12 Structures observed with SEM could be linked with lower hierarchy
13 structures observed with TEM to enable a multi-scale mapping and to
14 establish a hierarchical model of RO membranes. Cross-sections of
15 FIB-SEM reconstructions can be correlated to TEM micrographs
16 (compare Figure 1C with Figure 4A and Figure 5A). It is important to
17 note that FIB-SEM has limited capability to resolve the internal
18 structures in the PA layer (i.e., stacked membrane folds or smaller
19 voids), due to small contrast variations between the internal regions.
20 Therefore, we propose FIB-SEM should be utilised as a tool to
21 estimate the structural properties of the PA layer envelope (the
22 volume within the external surface of the PA layer).

23 **4.2. Nano-scale effects of staining**

24 RuO₄ stains polymers that contain aromatic rings, amine/amide
25 groups or unsaturated carbohydrates [43]. While the bulk effects of
26 RuO₄ staining are well known and described [43], experiments using
27 RuO₄ to study permeation pathways into RO membranes, have not
28 previously been conducted. By analogy to polyethylene [44,45], we
29 suggest that RuO₄ would oxidise the carbonyl and amide groups of
30 polyamide. While this process alters the chemical composition of the
31 stained film, it fixes and stabilises the structure by forming additional

1 crosslinks between oxidised functional groups. RuO_4 will move
2 through the polymer network until it oxidises one of the chemical
3 groups, limiting the pathway for diffusion of other molecules. At this
4 stage, precipitates (larger clusters of ruthenium oxides) will form
5 within the PA film. Therefore, the stain propagation is expected to be
6 a function of diffusion and reactivity within the PA film. Upon
7 membrane hydration, the staining of the film became more extensive
8 (Figure 4D, Figure 7B, Figure 5B). In the aqueous environment, the
9 PA film swells and enables further stain propagation within the
10 membrane, facilitated by RuO_4 -water interactions.

11

12 Nanocrystals of RuO_2 were also found to precipitate on external
13 surfaces of the polymer [46]. This phenomenon occurs for all
14 staining conditions (wet and dry) and is expected upon reduction of
15 unstabilised RuO_4 . This process occurs alongside the film staining
16 and increases with exposure time (SI Figure 7). A short exposure of 1
17 min was selected to provide suitable contrast to image the
18 nanostructure of the PA film.

19

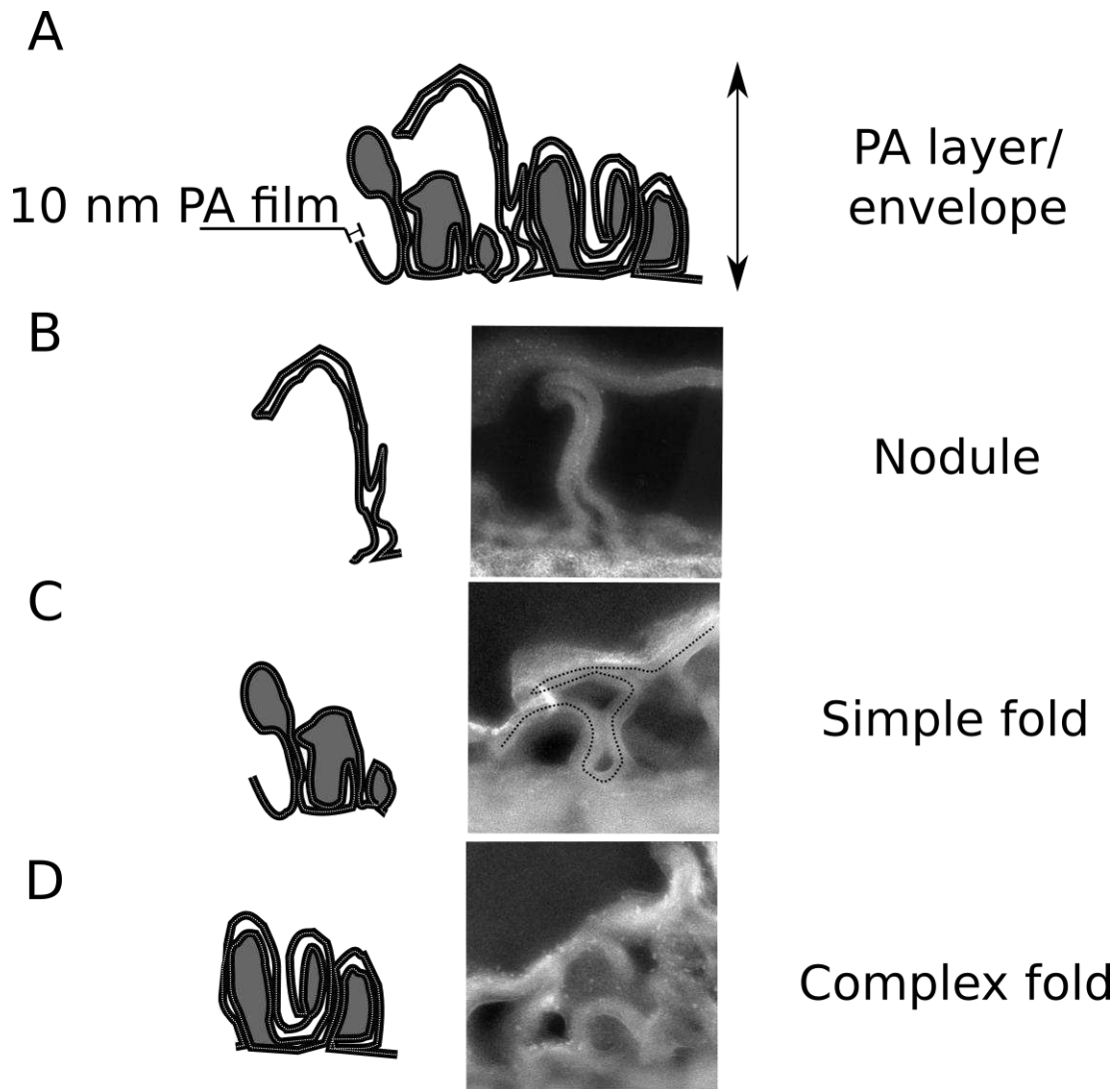
20 At higher magnification, TEM images of the PA layer cross-sections
21 revealed the presence of “channels” within the PA structure. These
22 structures were identified as hollow regions, possibly formed by tight
23 folding of the PA film. The presence of “channels” was further
24 confirmed by wet staining experiments. Staining patterns (Figure 5)
25 suggest that many of the finger-like structures observed in the TEM
26 images should be considered as “deflated balloons” rather than solid
27 nodules. Staining of each individual “channel” may vary depending
28 on its openness. Empty “channels” would be visible if the surrounding
29 membranes hindered all diffusing RuO_4 . Filled “channels” would
30 form if some of the RuO_4 passed through the PA film without
31 oxidation of any functional group in the PA network and precipitated
32 in the “channel” space. Importantly, “channels” were observed not
33 only in the protuberances on the front side of the PA layer, but also in

1 the loops of the basal regions (Figure 5D). Regions, in which
2 “channels” are visible, might have been formed from a highly
3 crumpled single nano-film as suggested by Karan et al. [15]. In Figure
4 9, a schematic of features observed in the PA layer is shown.

5
6 A number of studies shows cave-like protuberances, which agrees
7 with the crumpled nano-film model [6,16,19]. However, not all of the
8 structures observed in the PA layer could be simply explained by film
9 crumpling. Some of the studies report the presence of discrete voids
10 [19,20]; in particular, Pacheco et al. [19] visualised these voids from
11 reconstructed electron tomograms and attributed formation of
12 discrete voids to the presence of aqueous droplets during interfacial
13 polymerisation processes. Studies, in which this explanation of void
14 formation was proposed previously [47,48], describe voids of
15 micrometre (or greater) in size - orders of magnitude higher than our
16 case.

17 The smallest voids reconstructed in our study were around 15 nm in
18 diameter. Pacheco et al. also omitted reconstructing smaller voids due
19 to difficulties with interpreting the contrast in the images and the
20 resolution limit of electron tomography [49,50]. Smaller voids were
21 definitely present, but it is not clear whether they were discrete or
22 interconnected. We have made the same observation of both discrete
23 and interconnected voids in our study. Future work using direct
24 electron detectors and phase plates in electron microscopes will
25 enable sufficient image resolution to establish whether some of these
26 voids are in fact interconnected and to generate more complete model
27 of the PA membrane.

28



1

2 **Figure 9** A schematic of features observed in 2-D cross-sections of
 3 **the PA layer. (A) A general schematic of the ridge-valley**
 4 **structure. Individual features: (B) a nodule, (C) simple fold and**
 5 **(D) a complex fold. STEM images show fragments of the PA layer**
 6 **from top to PSf interface (white dashed line). The black, solid line**
 7 **represents the 10 nm crumpled, but continuous (dotted line)**
 8 **nano-film. Regions in grey can be interpreted as discrete holes.**
 9 **White regions within the PA layer are interpreted as “channels”.**

10 **4.3. Sub-nanometer porosity**

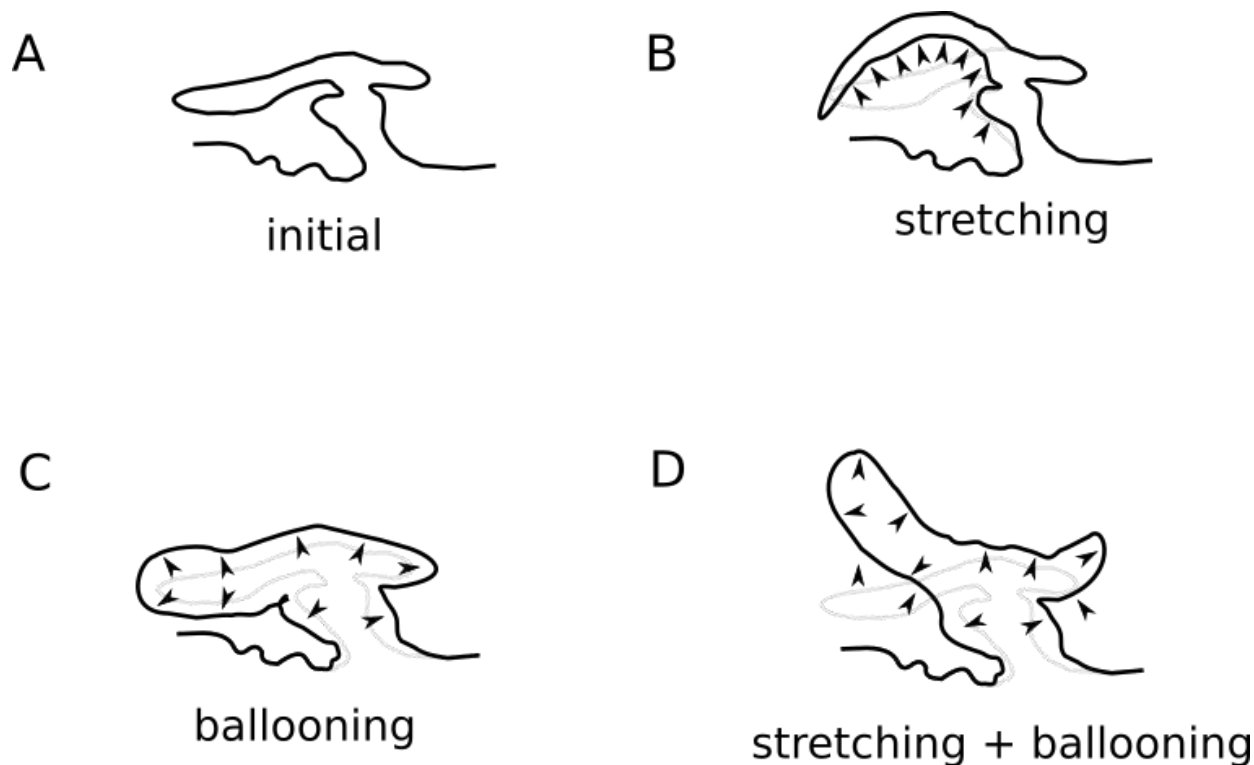
11 It has been suggested that nano-filtration through the membrane
 12 occurs within the PA nano-film itself as a result of sub-nanometre
 13 pores in the nano-film [4]. We attempted to visualise <1 nm diameter
 14 permeation pores within the PA nano-film by imaging the precipitates

1 using high resolution HAADF-STEM. The diameter of observed stain
2 precipitates within the PA nano-film matches the pore sizes estimated
3 with PALS [22,25,28] and calculated from molecular dynamics [26].

4 **4.4. Connections between structure and performance**

5 With the new data presented here we formulate a more accurate
6 hypothesis about the behaviour of the PA structures in the aqueous
7 environment. It was previously suggested that an increase in swelling
8 correlates with increased permeability in membranes [37]. The
9 reported swelling of the RO membranes (given as the difference
10 between the thickness of wet and dry membranes observed in AFM)
11 is usually in the range of 10-20 nm, possibly due to the rigidity of the
12 cross-linked, aromatic PA [20,37,41]. If we take into account the
13 morphology revealed by FIB-SEM, a few different mechanisms
14 should be considered. These mechanisms may involve external-
15 (stretching) and/or internally-driven (ballooning) expansion of the PA
16 structures. Tentative mechanisms of swelling are sketched in Figure
17 10.

18 In the present study, we were able to visualise the penetration of water
19 in the PA by using a stain tracer and elucidated the impact of water on
20 tracer transport within the PA. We concluded that not all of the PA
21 surfaces are immediately accessible and confirmed that water plays an
22 important role in activating the free volume of the PA layer and nano-
23 film. In the case of stain permeation, two effects can be observed: the
24 opening of <1 nm pores within the PA nano-film and the opening of
25 the larger voids, which may be considered discrete in the dry state,
26 within the PA layer. Both phenomena might, in turn, facilitate ion
27 permeation through the PA layer.



1

2 **Figure 10 Possible responses of the PA structures to the presence**
 3 **of water. (A) The initial dry state. (B) Stretching – water acts**
 4 **externally, elongating some structures, but preserving the original**
 5 **shape the PA layer. (C) Ballooning – water acts internal filling**
 6 **and expanding the free volume of the PA layer. (D) Combined –**
 7 **water acts externally and internally.**

8 **5. Conclusions**

9 In summary, the structural features of PA layer morphology in a
 10 representative RO membrane at the micro- and nano-scale have been
 11 visualised in 2-D and 3-D. The structural parameters of leaf-like
 12 sheets at the micro-scale were quantified. Their relation to the
 13 performance of membrane is discussed. Well-defined “channels”
 14 within the nodules, which have not previously been reported on, were
 15 imaged at the nano-scale. At the sub-nanometre scale, <1 nm pores
 16 were imaged. We believe our nano-scale results support the
 17 hypothesis that there is a nano-porous network underlying the
 18 filtration mechanics of the polyamide layer, which may be visualised
 19 using heavy metal staining. The staining in dry and wet conditions

1 also indicates the mechanism, by which water facilitates stain
2 permeation through the PA layer. Tomographic studies of stained
3 membranes provide new insight into the relationship between the
4 structure and the membrane performance and open new possibilities
5 for studying water flow and fouling in the vicinity of the PA layer in
6 silico.

7 **Acknowledgments**

8 This research was funded by the BP International Centre for
9 Advanced Materials (BP-ICAM). High resolution STEM imaging was
10 conducted at the SuperSTEM Laboratory, the U.K National Facility
11 for Aberration-Corrected STEM, supported by the Engineering and
12 Physical Sciences Research Council (EPSRC). We thank Prof.
13 Enrique Gomez for his helpful discussions.

14 **References**

- 15 [1] K.P. Lee, T.C. Arnot, D. Mattia, A review of reverse osmosis membrane materials for
16 desalination—Development to date and future potential, *J. Membr. Sci.* 370 (2011) 1–22.
17 doi:10.1016/j.memsci.2010.12.036.
- 18 [2] M. Elimelech, W.A. Phillip, The Future of Seawater Desalination: Energy, Technology, and the
19 Environment, *Science*. 333 (2011) 712–717. doi:10.1126/science.1200488.
- 20 [3] R.J. Petersen, Composite reverse osmosis and nanofiltration membranes, *J. Membr. Sci.* 83
21 (1993) 81–150.
- 22 [4] T. Uemura, K. Kotera, M. Henmi, H. Tomioka, Membrane technology in seawater desalination:
23 History, recent developments and future prospects, *Desalination Water Treat.* 33 (2011) 283–
24 288. doi:10.5004/dwt.2011.2646.
- 25 [5] D.G. Cahill, V. Freger, S.-Y. Kwak, Microscopy and microanalysis of reverse-osmosis and
26 nanofiltration membranes, *MRS Bull.* 33 (2008) 27–32.
- 27 [6] M. Kurihara, M. Hanakawa, Mega-ton Water System: Japanese national research and
28 development project on seawater desalination and wastewater reclamation, *Desalination*. 308
29 (2013) 131–137. doi:10.1016/j.desal.2012.07.038.
- 30 [7] C.Y. Tang, Y.-N. Kwon, J.O. Leckie, Probing the nano-and micro-scales of reverse osmosis
31 membranes—a comprehensive characterization of physiochemical properties of uncoated and
32 coated membranes by XPS, TEM, ATR-FTIR, and streaming potential measurements, *J. Membr.*
33 *Sci.* 287 (2007) 146–156.
- 34 [8] Y.-N. Wang, J. Wei, Q. She, F. Pacheco, C.Y. Tang, Microscopic Characterization of FO/PRO
35 Membranes – A Comparative Study of CLSM, TEM and SEM, *Environ. Sci. Technol.* (2012)
36 120827103647009. doi:10.1021/es301885m.
- 37 [9] S.-Y. Kwak, S.G. Jung, Y.S. Yoon, D.W. Ihm, Details of surface features in aromatic polyamide
38 reverse osmosis membranes characterized by scanning electron and atomic force microscopy,
39 *J. Polym. Sci. Part B Polym. Phys.* 37 (1999) 1429–1440.

- 1 [10] B. Mi, O. Coronell, B. Marinas, F. Watanabe, D. Cahill, I. Petrov, Physico-chemical
2 characterization of NF/RO membrane active layers by Rutherford backscattering spectrometry
3 ☆, *J. Membr. Sci.* 282 (2006) 71–81. doi:10.1016/j.memsci.2006.05.015.
- 4 [11] Q. Li, X. Pan, C. Hou, Y. Jin, H. Dai, H. Wang, X. Zhao, X. Liu, Exploring the dependence of bulk
5 properties on surface chemistries and microstructures of commercially composite RO
6 membranes by novel characterization approaches, *Desalination*. 292 (2012) 9–18.
7 doi:10.1016/j.desal.2012.02.005.
- 8 [12] V. Freger, A. Bottino, G. Capannelli, M. Perry, V. Gitis, S. Belfer, Characterization of novel acid-
9 stable NF membranes before and after exposure to acid using ATR-FTIR, TEM and AFM, *J.*
10 *Membr. Sci.* 256 (2005) 134–142.
- 11 [13] G.R. Guillen, Y. Pan, M. Li, E.M.V. Hoek, Preparation and Characterization of Membranes
12 Formed by Nonsolvent Induced Phase Separation: A Review, *Ind. Eng. Chem. Res.* 50 (2011)
13 3798–3817. doi:10.1021/ie101928r.
- 14 [14] F.A. Pacheco, I. Pinnau, M. Reinhard, J.O. Leckie, Characterization of isolated polyamide thin
15 films of RO and NF membranes using novel TEM techniques, *J. Membr. Sci.* 358 (2010) 51–59.
- 16 [15] S. Karan, Z. Jiang, A.G. Livingston, Sub-10 nm polyamide nanofilms with ultrafast solvent
17 transport for molecular separation, *Science*. 348 (2015) 1347–1351.
18 doi:10.1126/science.aaa1313.
- 19 [16] H. Yan, X. Miao, J. Xu, G. Pan, Y. Zhang, Y. Shi, M. Guo, Y. Liu, The porous structure of the fully-
20 aromatic polyamide film in reverse osmosis membranes, *J. Membr. Sci.* 475 (2015) 504–510.
21 doi:10.1016/j.memsci.2014.10.052.
- 22 [17] C. Kong, A. koushima, T. Kamada, T. Shintani, M. Kanezashi, T. Yoshioka, T. Tsuru, Enhanced
23 performance of inorganic-polyamide nanocomposite membranes prepared by metal-alkoxide-
24 assisted interfacial polymerization, *J. Membr. Sci.* 366 (2011) 382–388.
25 doi:10.1016/j.memsci.2010.10.026.
- 26 [18] T. Kamada, T. Ohara, T. Shintani, T. Tsuru, Optimizing the preparation of multi-layered
27 polyamide membrane via the addition of a co-solvent, *J. Membr. Sci.* 453 (2014) 489–497.
28 doi:10.1016/j.memsci.2013.11.028.
- 29 [19] F. Pacheco, R. Sougrat, M. Reinhard, J.O. Leckie, I. Pinnau, 3D visualization of the internal
30 nanostructure of polyamide thin films in RO membranes, *J. Membr. Sci.* (2015).
31 doi:10.1016/j.memsci.2015.10.061.
- 32 [20] L. Lin, R. Lopez, G.Z. Ramon, O. Coronell, Investigating the void structure of the polyamide
33 active layers of thin-film composite membranes, *J. Membr. Sci.* 497 (2016) 365–376.
34 doi:10.1016/j.memsci.2015.09.020.
- 35 [21] J.G. Wijmans, R.W. Baker, The solution-diffusion model: a review, *J. Membr. Sci.* 107 (1995)
36 1–21.
- 37 [22] T. Fujioka, N. Oshima, R. Suzuki, W.E. Price, L.D. Nghiem, Probing the internal structure of
38 reverse osmosis membranes by positron annihilation spectroscopy: Gaining more insight into
39 the transport of water and small solutes, *J. Membr. Sci.* 486 (2015) 106–118.
40 doi:10.1016/j.memsci.2015.02.007.
- 41 [23] S. Li, Z. Wang, C. Zhang, M. Wang, F. Yuan, J. Wang, S. Wang, Interfacially polymerized thin film
42 composite membranes containing ethylene oxide groups for CO₂ separation, *J. Membr. Sci.*
43 436 (2013) 121–131. doi:10.1016/j.memsci.2013.02.038.
- 44 [24] J. Albo, J. Wang, T. Tsuru, Gas transport properties of interfacially polymerized polyamide
45 composite membranes under different pre-treatments and temperatures, *J. Membr. Sci.* 449
46 (2014) 109–118. doi:10.1016/j.memsci.2013.08.026.
- 47 [25] A. Shimazu, H. Goto, T. Shintani, M. Hirose, R. Suzuki, Y. Kobayashi, Vacancy profile in reverse
48 osmosis membranes studied by positron annihilation lifetime measurements and molecular
49 dynamics simulations, *J. Phys. Conf. Ser.* 443 (2013) 012050. doi:10.1088/1742-
50 6596/443/1/012050.

- 1 [26] V. Kolev, V. Freger, Hydration, porosity and water dynamics in the polyamide layer of reverse
2 osmosis membranes: A molecular dynamics study, *Polymer*. 55 (2014) 1420–1426.
3 doi:10.1016/j.polymer.2013.12.045.
- 4 [27] M. Doi, S.F. Edwards, *The Theory of Polymer Dynamics*, Oxford : Clarendon, 1986.
- 5 [28] M. Henmi, Y. Fusaoka, H. Tomioka, M. Kurihara, High performance RO membranes for
6 desalination and wastewater reclamation and their operation results, *Water Sci. Technol.* 62
7 (2010) 2134. doi:10.2166/wst.2010.396.
- 8 [29] K. Košutić, L. Kaštelan-Kunst, B. Kunst, Porosity of some commercial reverse osmosis and
9 nanofiltration polyamide thin-film composite membranes, *J. Membr. Sci.* 168 (2000) 101–108.
- 10 [30] J. Stawikowska, A.G. Livingston, Nanoprobe imaging molecular scale pores in polymeric
11 membranes, *J. Membr. Sci.* 413-414 (2012) 1–16. doi:10.1016/j.memsci.2012.02.033.
- 12 [31] R.W. Baker, *Reverse Osmosis*, in: *Membr. Technol. Appl.*, 2nd ed, J. Wiley, Chichester ; New
13 York, 2004: pp. 191–235.
- 14 [32] M. Doube, BoneJ, (n.d.). <http://bonej.org/thickness>.
- 15 [33] W.S. Rasband, ImageJ, (1997). <http://imagej.nih.gov/ij/>.
- 16 [34] M. Doube, M.M. Klosowski, I. Arganda-Carreras, F.P. Cordelières, R.P. Dougherty, J.S. Jackson,
17 B. Schmid, J.R. Hutchinson, S.J. Shefelbine, BoneJ: Free and extensible bone image analysis in
18 ImageJ, *Bone*. 47 (2010) 1076–1079. doi:10.1016/j.bone.2010.08.023.
- 19 [35] T. Hildebrand, P. Ruegsegger, A new method for the model-independent assessment of
20 thickness in three-dimensional images, *J. Microsc.* 185 (1997) 67–75.
- 21 [36] C.M. McGilvery, A.E. Goode, M.S.P. Shaffer, D.W. McComb, Contamination of holey/lacey
22 carbon films in STEM, *Micron*. 43 (2012) 450–455. doi:10.1016/j.micron.2011.10.026.
- 23 [37] V. Freger, Swelling and Morphology of the Skin Layer of Polyamide Composite Membranes: An
24 Atomic Force Microscopy Study, *Environ. Sci. Technol.* 38 (2004) 3168–3175.
25 doi:10.1021/es034815u.
- 26 [38] A.K. Ghosh, B.-H. Jeong, X. Huang, E.M.V. Hoek, Impacts of reaction and curing conditions on
27 polyamide composite reverse osmosis membrane properties, *J. Membr. Sci.* 311 (2008) 34–45.
28 doi:10.1016/j.memsci.2007.11.038.
- 29 [39] M.L. Lind, A.K. Ghosh, A. Jawor, X. Huang, W. Hou, Y. Yang, E.M.V. Hoek, Influence of Zeolite
30 Crystal Size on Zeolite-Polyamide Thin Film Nanocomposite Membranes, *Langmuir*. 25 (2009)
31 10139–10145. doi:10.1021/la900938x.
- 32 [40] J. Yin, E.-S. Kim, J. Yang, B. Deng, Fabrication of a novel thin-film nanocomposite (TFN)
33 membrane containing MCM-41 silica nanoparticles (NPs) for water purification, *J. Membr. Sci.*
34 423-424 (2012) 238–246. doi:10.1016/j.memsci.2012.08.020.
- 35 [41] E. Dražević, K. Košutić, V. Freger, Permeability and selectivity of reverse osmosis membranes:
36 Correlation to swelling revisited, *Water Res.* 49 (2014) 444–452.
37 doi:10.1016/j.watres.2013.10.029.
- 38 [42] J. Lee, A. Hill, S. Kentish, Formation of a thick aromatic polyamide membrane by interfacial
39 polymerisation, *Sep. Purif. Technol.* 104 (2013) 276–283. doi:10.1016/j.seppur.2012.11.015.
- 40 [43] J.S. Trent, J.I. Scheinbeim, P.R. Couchman, Ruthenium tetroxide staining of polymers for
41 electron microscopy, *Macromolecules*. 16 (1983) 589–598.
- 42 [44] H. Sano, T. Usami, H. Nakagawa, Lamellar morphologies of melt-crystallized polyethylene,
43 isotactic polypropylene and ethylene-propylene copolymers by the RuO₄ staining technique,
44 *Polymer*. 27 (1986) 1497–1504.
- 45 [45] H. Haubruge, A. Jonas, R. Legras, Staining of poly(ethylene terephthalate) by ruthenium
46 tetroxide, *Polymer*. 44 (2003) 3229–3234. doi:10.1016/S0032-3861(03)00255-6.
- 47 [46] T.M. Chou, P. Prayoonthong, A. Aitouchen, M. Libera, Nanoscale artifacts in RuO₄-stained poly
48 (styrene), *Polymer*. 43 (2002) 2085–2088.
- 49 [47] L.J.J.M. Janssen, K. te Nijenhuis, Encapsulation by interfacial polycondensation. I. The capsule
50 production and a model for wall growth, *J. Membr. Sci.* 65 (1992) 59–68.

- 1 [48] F. Yuan, Z. Wang, X. Yu, Z. Wei, S. Li, J. Wang, S. Wang, Visualization of the Formation of
2 Interfacially Polymerized Film by an Optical Contact Angle Measuring Device, *J. Phys. Chem. C.*
3 116 (2012) 11496–11506. doi:10.1021/jp210209v.
- 4 [49] P.A. Midgley, R.E. Dunin-Borkowski, Electron tomography and holography in materials science,
5 *Nat. Mater.* 8 (2009) 271–280. doi:10.1038/nmat2406.
- 6 [50] C.A. Diebolder, A.J. Koster, R.I. Koning, Pushing the resolution limits in cryo electron
7 tomography of biological structures: PUSHING THE RESOLUTION LIMITS IN CRYO ELECTRON
8 TOMOGRAPHY, *J. Microsc.* 248 (2012) 1–5. doi:10.1111/j.1365-2818.2012.03627.x.

9

10

11